Hyperspectral Imaging Polarimeter (HIP) Observations of Ice Clouds: Data and Modeling[1]

C.J. Beeler, S.A. Rappaport, P.C. Joss, J. Devore, A.J. LePage, A.T. Stair, Jr.
Visidyne, Inc.
10 Corporate Place
South Bedford Street
Burlington, MA 01803
(978) 273-2820
beeler@visidyne.com, sar@mit.edu, joss@mitlns.mit.edu,
devore@visidyne.com, lepage@visidyne.com, ats@visidyne.com

J.A. Kristl
Stewart Radiance Laboratory
SDL/USU
139 The Great Road
Bedford, MA 01730
jkristl@sdl.usu.edu

M. Greenman, G. Jensen, J. Peterson
Space Dynamics Laboratory/ Utah State University
1695 North Research Parkway
North Logan, UT 84341-1947
markg@sdl.usu.edu, gary.jensen@sdl.usu.edu, james.peterson@sdl.usu.edu

Abstract—In support of the RAMOS (*R*ussian *Am*erican *O*bservation *S*atellites) program, an ongoing series of flights is being conducted using FISTA (*F*lying *I*nfrared *S*ignatures *T*echnology *A*ircraft) which, in part, carries instruments to obtain polarization measurements of solar radiation scattered from clouds. Spectral polarization measurements have been made simultaneously across the 2.5-3.5 μm region as a function of solar scattering angle using the Space Dynamics Laboratory's Hyperspectral Imaging Polarimeter (HIP) instrument. The purpose of the experiment is to verify the expected strong sensitivity of polarization as a function of wavelength within this spectral band, and to select the optimum wavelength for making remote diagnostic measurements of cloud compositions. There is also the complementary goal of studying polarization as a potential discriminator between naturally occurring solar-scatter backgrounds and man-made objects.

Additional instrumentation onboard during these flights have indicated that the clouds present in these observations were composed primarily of ice rather than water. This paper is therefore focused on our efforts to model polarization due to solar scattering from non-spherical ice crystals. We describe the FISTA experiment, the HIP instrumentation, and the data processing methods used to derive the polarization data products. Finally, we present a simulation of the FISTA polarization experiment and compare these modeled results to the HIP data themselves.

TABLE OF CONTENTS

1. INTRODUCTION

In 1997 and 1998 a series of flights were made using the FISTA aircraft to obtain polarization measurements of solar radiation scattered from clouds over a range of infrared wavelength bands simultaneously. Such flights have recently been repeated in 1999 and are expected to continue in 2000. The immediate purpose of these investigations is to obtain the data required to characterize the polarization properties of various atmospheric phenomena with applications toward background clutter mitigation, the ability to differentiate between clouds of various compositions (e.g., ice versus water clouds), and the verification of theoretical polarization models.

Polarization models based on single scattering theory indicate that differences in cloud composition can be best

---

determined by making polarization measurements at wavelength bands that correspond to the shoulders of infrared absorption bands of ice and liquid water. The Space Dynamics Laboratory (SDL) at Utah State University has built a Hyperspectral Imaging Polarimeter (HIP) specifically for these measurements. The HIP spectral range is approximately 2.5 – 3.5 μm.

Ultimately these polarization measurements and models will be used to design instruments, choose appropriate wavelength bands, and plan experiments for future air- and space-based instrument platforms such as those envisioned for RAMOS.

In this paper we briefly review polarization principles of light scattered from clouds, describe the HIP polarization experiment, and present the results of a Monte Carlo scattering model we developed to compare with the polarization data.

2. THEORY

The degree and angle of linear polarization of radiation scattered by clouds in the infrared absorption bands of water (e.g. at 3 μm) can be measured by use of aircraft, satellites, or ground-based instrumentation. Such measurements have at least two potentially important applications which are currently the subject of a patent application by Visidyne, Inc. First, this technique affords a method of discriminating between clouds and other sources of radiation, and can thus provide a potentially powerful technique for clutter mitigation. Second, the polarization signature contains substantial information regarding the phase (water, ice, or a mixture) of the particles at cloud surfaces.

There are certain types of clouds that are of particular interest for carrying out polarization measurements. These include:

(a) Clouds that are known to be composed either entirely of water droplets or ice crystals. Since the phase of the cloud particles is known, the measured polarization signals can be used to provide empirical confirmation of the signals predicted theoretically for each particle type.

(b) Mixed-phase clouds, particularly those that may contain regions of highly supercooled water droplets. The most easily identifiable clouds of this type will be clouds associated with thunderstorms in their formative stages. We note that such clouds have a great deal of vertical structure. Therefore, if they are viewed from an oblique angle relative to the local nadir, considerable information concerning the phase of the cloud particles as a function of altitude may be gained, even though only scattering from the outer surface of the cloud can be measured.

Information regarding the phase of the cloud particles, combined with data on the altitude of the cloud tops, has, in

turn, a number of potentially important scientific applications. In particular, determination of the glaciation level in clouds via remote sensing techniques would be of considerable importance to aviation interests, for use in numerical weather prediction, and for incorporation into global climate models.

Cloud Polarization

Let $P(\theta_S, \theta_0, \varphi_0)$ and $A(\theta_S, \theta_0, \varphi_0)$ be the degree of linear polarization and the direction of the polarization vector (relative to some reference direction), respectively, for radiation incident from a source of unpolarized light (such as sunlight at polar angle θ_S in the y-z plane) and scattered by a cloud element at the origin toward an observer in the direction θ_0, φ_0, where the $+z$-axis is the zenith direction, as shown in Figure 1. Also note the solar scattering angle (SCA), labeled α in the figure.
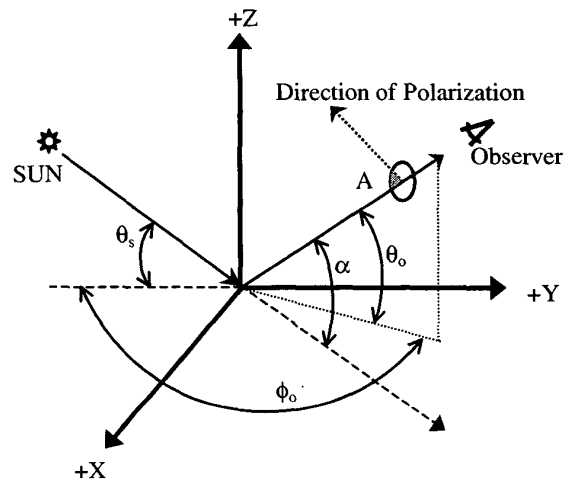

Figure 1. Definition of angles

In general, both P and A depend on all of the following factors:

1. The spatial orientation of the upper surface of the cloud.
2. The phase of the cloud particles.
3. The distribution of the shapes, sizes, and spatial orientations of the cloud particles.

The phase of cloud particles affects P and A through the index of refraction and the absorptive properties of the particles. The real part of the index of refraction differs only slightly between water and ice and is, in any event, easily accounted for in calculations of P and A. However, the absorptive properties of the particles substantially complicate the necessary calculations. For ice, in particular, the imaginary part of the index of refraction (which is closely related to the absorption length) varies by about six orders of magnitude in the short-wave infrared (SWIR) and is uncertain at any given wavelength to about a factor of 2.

For the case of water clouds, the droplets are spherical, so that the problem can be treated according to the theory of Mie scattering, which is well-developed [1]. Here, P and A are functions only of α. The greatest complication for the calculation of $P(\alpha)$ for water clouds arises from the distribution of droplet sizes within the cloud. This distribution varies considerably from one type of cloud to another and is imperfectly known for any type of cloud.

The calculation of both P and A is much more complicated for ice clouds than for water clouds, since the ice crystals comprising the clouds can take on a variety of shapes. The basic symmetry of ice crystals is hexagonal but, within this constraint, a wide variety of shapes are possible, including plates, columns, and double pyramids, all with a wide range of possible ratios among the principal axes [2,3,4]. Individual crystals may also fuse together in a wide and complex variety of ways. A given cloud may thus be composed of individual crystals and/or crystal clusters with a variety of shapes and a range of sizes and spatial orientations for each shape.

As a consequence of these complications, even for a specified distribution of crystal shapes, sizes, and orientations, P and A are no longer functions of α alone. Nevertheless, those computational results that exist for the degree of polarization of radiation scattered from ice clouds are generally averaged appropriately over θ_S, θ_0, and φ_0 and presented as functions of α only [4,5]. Nearly all of the existing calculations of P for ice clouds apply to visual wavelengths only. A few results are available for SWIR wavelengths [4,5] and provide encouraging evidence that

measurements at such wavelengths can, indeed, yield useful information about the nature of the cloud particles.

Theoretical Approach

Even in the simplest cases, the treatment of polarization of radiation scattered from clouds requires extensive numerical computations. Two techniques have been developed for such computations: the "doubling method" [6] and Monte Carlo techniques [1].

While large fractional polarization occurs for many scattering geometries for single scattering, the randomizing effect of multiple scattering will significantly reduce P. Thus one objective is to maximize the contribution of singly scattered photons in the measured signal. One way to do this is to choose a wavelength at which the scattering particles are highly absorbing.

As noted in the previous section, the imaginary component of the index of refraction, n_i, of a substance is a direct measure of how strongly that substance absorbs electromagnetic radiation. Figure 2 illustrates the variation of n_i for water and ice as a function wavelength, λ, from 2 to 6 μm, as measured experimentally by Hale and Querry [7] and by Schaaf and Williams [8]. Note that for both water and ice, the maximum values of n_i occur in the range of about 2.8 to 3.3 μm, with a more modest peak centered near 4.8 μm for water and 4.5 μm for ice.
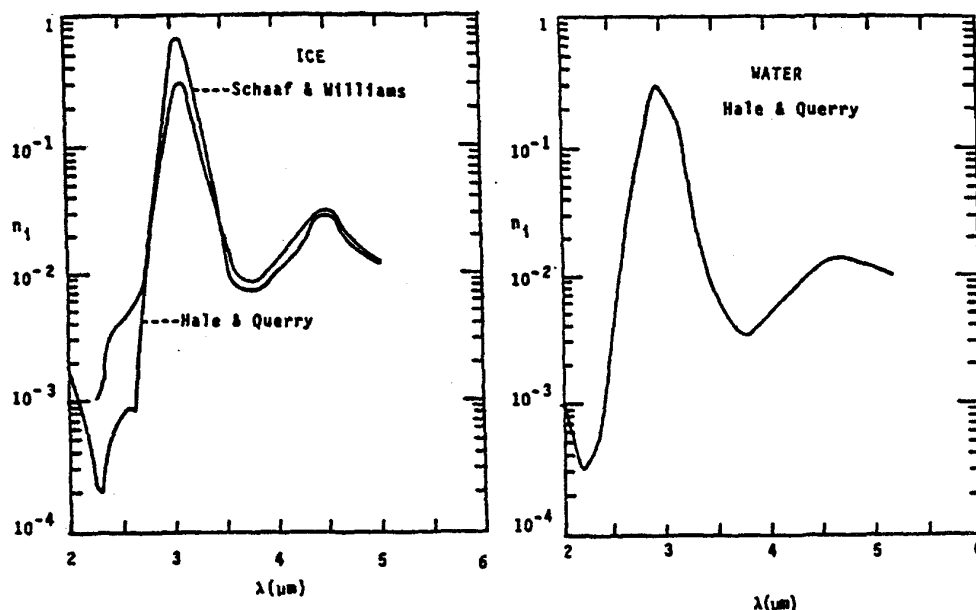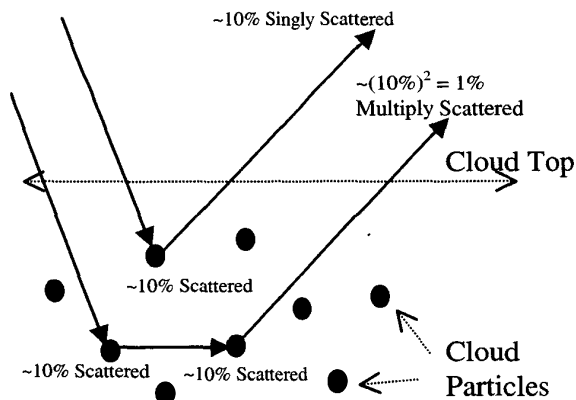

Figure 2. The imaginary part of the index of refraction for water and ice as a function of wavelength [7,8]

Once it enters the cloud top, a light ray may be scattered by a water droplet or ice particle, or it may be absorbed by such a particle or by the water vapor in the saturated air between particles. Note, however, that the SWIR absorption band for water vapor is at somewhat shorter wavelengths, about 2.6 to 2.8 μm, than the absorption bands for liquid water or solid ice.

Let r be the ratio, per particle-light ray interaction, of the probability of scattering to the probability of absorption. Absorption can be either by the particle or by the intervening water vapor, along the path traversed by the ray since entering the cloud top or since the previous interaction of the ray with a particle.

While the amount of scattered radiation in a band selected such that r . 10% throughout the band will be more than adequate for the measurement of P and A, the fraction of *incident* light rays that are doubly (or multiply) scattered and still escape from the cloud top without being absorbed will be of the order of $(10\%)^2$, or about 1%. As a result the percentage of the radiation *reaching the detector* that has undergone more than one scattering event will be $\sim(10\%)^2/10\%$ or about 10%, as shown schematically in Figure 3. Thus, the great majority of the rays reaching the detector will have undergone only a single scattering at the cloud top, so that the light reaching the detector will generally have a high degree of linear polarization.

Figure 3. Schematic of the scattering within a cloud

~10% Singly Scattered

$\sim(10\%)^2 = 1\%$
Multiply Scattered

Cloud Top

~10% Scattered

~10% Scattered   ~10% Scattered

Cloud
Particles

3. INSTRUMENTATION

Flying Infrared Signatures Technology Aircraft

The FISTA aircraft is a modified NKC-135E aerial refueling tanker (serial number 55-3135) built by Boeing that is based with the 452nd Test Squadron at Edwards AFB, California. It has a continuous flying time of 11 hours, a maximum range of about 11,000 km, and a maximum ceiling of 13,000 meters.

FISTA has been modified to act as a test bed for a wide variety of infrared and visible sensor systems. It has 20 windows on the starboard side of the fuselage with nearly all consisting of a 31.8 cm diameter clear aperture which are either filled by a clear 1.9 cm thick Lexan window, and an instrument window, or periscope. Provisions also exist to mount periscopes in selected windows, which allow the instrument to look in a variety of directions including fore, aft, up, and down.

The aircraft is also equipped with a GPS (Global Positioning System) to provide data on the position, heading and speed of the aircraft as well as its attitude. All these data along with a GPS-derived time base are recorded for later use in interpreting the data and calculating scattering angles.

Hyperspectral Imaging Polarimeter

HIP is a proof-of-concept sensor, combining hyperspectral pushbroom imaging with high speed, solid state polarimetry [9]. The sensor was designed using as many off-the-shelf components as possible, and utilizes an optical breadboard design for rapid prototyping. It is based around a 256 × 320 window-selectable InSb camera, a solid-state ferroelectric liquid crystal (FLC) polarimeter, and a reflective diffraction grating. It was designed for installation and operation on FISTA and was formally approved as a Class II aircraft modification in May 1998. Figure 4 shows a photograph of the sensor.

The HIP instrument measures a narrow (160 × 1 pixel) vertical field-of-view (FOV) with an IFOV (instantaneous field-of-view) of approximately 1.2 H 1.2 mrad. The scene is scanned with this FOV using the forward motion of the aircraft (pushbroom operation). Each of the 160 spatial elements has a 96-element spectrum (2.5 - 3.5 μm) from which the total radiance, the percentage of the total that is linearly polarized, and the linear polarization angle can be derived. With accurate knowledge of the instrument pointing and the aircraft platform speed, hyperspectral images can be constructed from the HIP measurements.

The hyperspectral portion of the HIP sensor is a standard spectrometer with a slit and a dispersive grating. The optical elements of the system consist of:

1. The front-end slit re-imaging optics, made by Diversified Optics, Inc. A pair of IR doublets and a 50 μm × 7.6 mm slit define the spectrometer slit in one dimension, and the field slit in the other.
2. The solid state polarimeter stack.
3. The gold reflective diffraction grating, a 75 g/mm grating blazed at 4.65 μm from Richardson Grating Laboratory.
4. The IR camera lens is an off-the-shelf 25-mm lens, also built by Diversified Optics, Inc.

5. The IR camera is a 256 × 320 InSb camera built by Santa Barbara Focalplane (SBF), of California. The camera focal plane array is windowable, allowing smaller sub-areas of the array to be selected and read out.
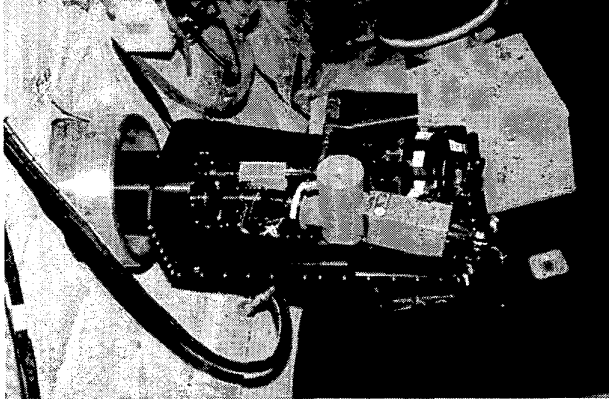

Figure 4. HIP System Installed on FISTA

For the FISTA98 flights, the HIP used only a 96 × 160 detector area of the array. This allowed for considerable savings in data recording and handling capabilities. The windowing capability of the camera will allow for the HIP system to be modified and optimized for differing measurement scenarios. The 14-bit digitized samples are reported in 16-bit integer words.

HIP uses a polarimeter design based around FLC cells, a patented design made by Displaytech, Inc., of Boulder, Colorado. These devices are commonly used for light shutters, but have also been shown suitable as the basis for a high-speed polarimeter [10]. Ferroelectric liquid crystals are linear polarization half-wave retarders that can be electrically switched between two optic-axis rotational states. By reversing the voltage across the smectic liquid crystal material, the optic axis is rotated through 45 degrees in less than 3 milliseconds.

The co-aligned video camera records a visible band image of the target scene, with a reticle inserted to help locate the position of the infrared line being imaged. Three ring-laser rate gyros are mounted in an orthogonal configuration, with one axis closely aligned with the camera optical axis. The gyro information can be used in conjunction with the FISTA onboard GPS positioning and attitude system to accurately compute the pointing of HIP during an experiment, and the consequent footprint and scattering angles of each pixel sample.

HIP Polarization Data Processing

The desired HIP polarization measurements are the degree and angle of linear polarization, as well as the total intensity of the sunlight scattered off uniform cloud decks. The optimum configuration of a polarization analyzer for deriving the linear Stokes parameters is a linear polarizer with measurement rotation angles of 0, 60, and 120 degrees. This configuration provides a symmetric response that allows the Stokes parameters of the incident beam to be accurately derived using only three measurement rotation angles. Unfortunately FLC technology does not provide these angles. Because of this hardware limitation, the HIP uses measurement rotations of 0, 45, 90, and −45 degrees. These measurement angles also provide good symmetry but require one additional measurement. Thus, four complete focal plane images must be collected in order to make a single polarization measurement [11,12,13].

The components used to create the various measurement rotation angles are (see Figure 5):

1. A half-wave FLC with fast axis orientations of 0° (unswitched) and 45° (switched).
2. A quarter-wave FLC with fast axis orientations of 0° (unswitched) and 45° (switched).
3. A quarter-wave fixed retarder with the fast axis set to 45°.
4. A wire-grid, linear polarizer aligned horizontally.

We define modified linear Stokes parameters, which completely describe the linear polarization characteristics of the incident beam and are used to compute the degree and angle of linear polarization. These parameters consist of three components, the source intensity *(I)* and the orthogonal polarization parameters, *Q* and *U*. The parameter *Q* is the intensity difference between horizontal (polarization angle of zero degrees) and vertical (polarization angle of 90 degrees) linear polarization. The parameter *U* is the intensity difference between linear polarization at positive 45 degrees and negative 45 degrees. The parameter *I* is the sum of the intensities at polarization angles 0 and 90 degrees.

The degree, *P*, and angle, *A*, of linear polarization and the total intensity can be determined from the modified Stokes parameters:

$$P = \frac{\sqrt{Q^2 + U^2}}{I_{Tot}}, \qquad (1)$$

$$A = \frac{1}{2}\tan^{-1}(\frac{U}{Q}), \qquad (2)$$

where

$$I_{Tot} = I(0°) + I(90°). \qquad (3)$$

Note that equation (1) is the definition of percent *total* polarization (linear *and* circular); however, since the contribution of circular polarization in nature is generally very small in comparison to that of linear polarization, we assume it to be zero and refer to this definition as fractional *linear* polarization. Before computing the Stokes vector corresponding to a measurement set in each state of the HIP polarization stack (-45, 0, 45, and 90 degrees), the measured

responses must be converted from the raw pixel responses read out from the HIP focal plane into a measured flux [14].
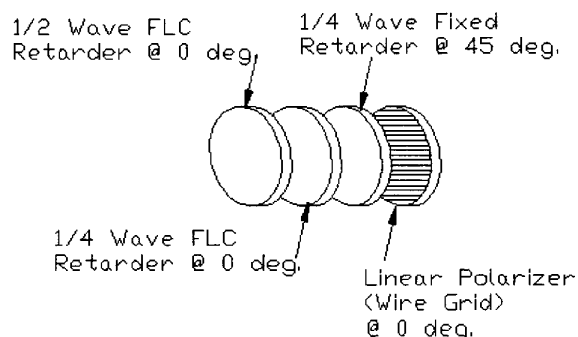

Figure 5. Polarizer Components Used to Measure Different Polarization Vectors

Maximizing the signal to noise level is important for the HIP measurements. Low signal levels compared to the noise are especially problematic for HIP in determining the degree of polarization. Custom software was developed to process the HIP data from its raw form to calibrated hypercubes for each of intensity, degree of polarization, and angle of polarization. This software was written at SDL in C++ and runs on PCs under the Windows NT® 4.0 operating system. In addition to several operations including the detection, flagging or removal of non-optimum performing pixels, offset correction, responsivity application, polarization set formation, Stokes parameter computation, and formatting, the post-processing software also performs the following key data processing steps:

Time-dimension coadding: The samples from a specified number of polarization sets can be averaged together. The polarization set is averaged independently for each pixel. Processing with the time coadding factor set to 1 set (i.e., no coadding), 10 sets, 20 sets, and 40 polarization sets were each tried for selected data from the 1998 series of flights.

Spatial-dimension coadding: The Stokes vectors from a specified number of pixels in the same focal plane column, in the same band, can be averaged together. Processing with the spatial coadding factor set to 1 row (i.e., no coadding), 10 rows, 20 rows, and 70 rows were each tried for selected data from the 1998 series of flights.

These two coadding processes are essential for the HIP data in order to sufficiently increase the signal to noise level so that meaningful polarization parameters can be derived. The data presented in this paper have been both spatially (70 pixels) and temporally (40 frames) coadded.

4. HIP DATA

One goal of the polarization measurements was to measure the polarization fraction of the scattered sunlight as a function of solar scattering angle. The scattering angle, α, as mentioned earlier, is the angle between the sun-to-cloud vector and the cloud-to-observer vector, Figure 6a. An illustration of the viewing geometry of the experiment is provided in Figure 6b below. The flight trajectories were designed to maximize the scattering angle coverage. This required late afternoon (or early morning) flights, with low solar elevation. As the SCA (α) goes to zero this represents the forward scattering case. The largest scattering angle occurs when the sun is behind FISTA, here $\alpha = 180 - |\theta_s - \theta_a|$, which corresponds to something close to the backscatter case. In practice, the scattering angle does not go to zero because this would require the line-of-sight (LOS) to be pointed directly at the sun. A minimum in solar elevation, corresponding to the shallow bank angle used on FISTA, extends the smallest scattering angle that can be attained during an orbit.
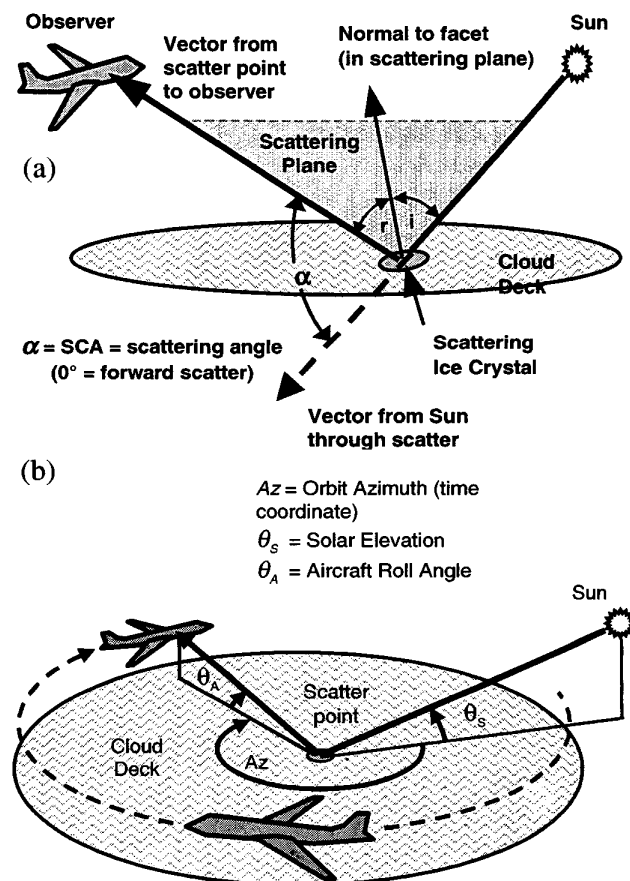

Figure 6. Illustrations of the a) Scattering Plane Geometry and b) Experiment Geometry

378

The FISTA orbited around a fixed point on the cloud, using a right bank of 5 to 30 degrees such that the LOS elevation matched the solar elevation. Large extended cloud decks were selected so that the polarimeter FOV would remain on the cloud during the entire orbit regardless of winds. Flight locations were selected based on the likely presence of extended cloud formations at altitudes of 25,000 feet or more. Once the FISTA entered the area, the clouds were visually evaluated, and then an orbit was set up around the cloud deck selected for measurement.

A Tans Vector GPS system gives location, speed, and heading of the FISTA. It also measures the aircraft roll, pitch, and yaw continuously through each orbit. This allows the measurement geometry to be determined after the flight to within a few degrees accuracy for the sensors which remain in a fixed orientation with respect to the aircraft. The FISTA-to-cloud range was measured using PEELS (Portable Eyesafe Environmental Lidar System); and this can be combined with the measurement geometry to determine the cloud altitude.

A quick-look survey performed soon after the completion of the FISTA98 experiments suggested that the best signal levels would be obtained from the side-looking 9903 flight. The HIP data processing and analysis have therefore concentrated on the events from this flight. The results reported in this paper are limited to Event 3 data.

Figure 7 shows the total intensity, angle of polarization, and percent polarization, respectively, plotted against solar scattering angle (SCA) in the 2.49 μm channel. In each of the three plots, the triangles and squares are data from detectors 0 and 1 respectively. These "detectors" are the result of the spatial coaddition of 70 pixels as well as temporal coaddition of 40 frames, as described in the previous section. During the course of one FISTA orbit, the range of SCA's is cycled through twice. The two cycles are distinguished in these figures by color (red versus blue). The solid curves are the results of our modeling which will be discussed in the next section. As seen in Figure 7a, the total intensity decreases by approximately two orders of magnitude from the near-forward scattering angles toward the backscatter geometry.

The shape of the polarization angle curve as a function of SCA (see Figure 7b) is determined almost entirely by the geometry of the observation. The orbiting motion of the sensor relative to the scatter point causes the scattering plane to rotate/tilt in such a way that it generates a range of polarization angles that range from approximately –90 to +90 degrees. It is interesting to note here that the two cycles of SCA should appear as a separation of color between the lower and upper halves of this curve. Any mixture of the two colors is probably indicative of a low signal to noise ratio.

Figure 7c shows the percent polarization as a function of SCA in the 2.49 μm spectral channel. By following the
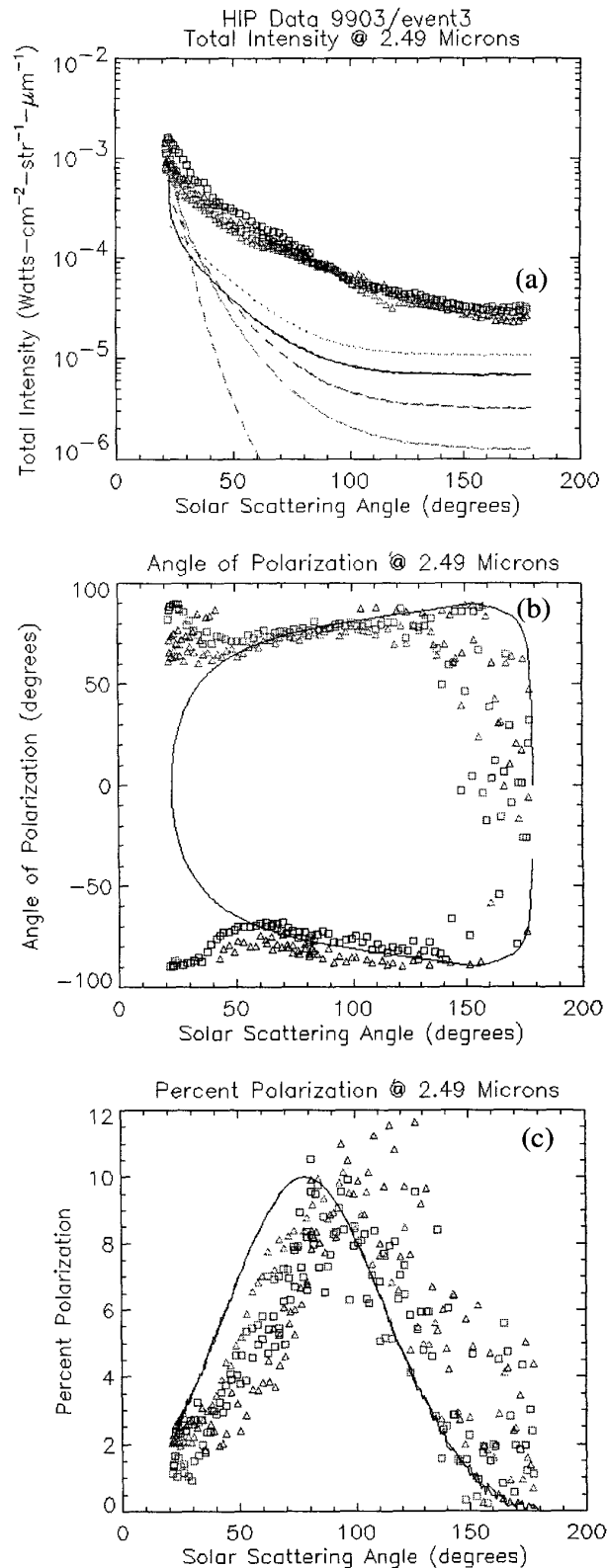

Figure 7. HIP Data at 2.49 μm: a) Total Intensity, b) Angle of Polarization, c) Percent Polarization

curve within one detector and color, one can distinguish between the two halves of the orbit. The data seem to peak at a maximum polarization of about 10% near 90 degrees SCA, however both halves of the orbit do not necessarily peak at the same place, and the scatter in the data is quite large. This latter observation can be explained by the fact that during the orbit, the operators attempted to point the sensor at the same cloud feature (a difficult task) and were not always successful. The percent polarization data at this wavelength are somewhat better behaved than for the data in other bands.

Figure 8 contains the same types of results as shown in Figure 7 with the exception that they represent data recorded in the 3.01 μm channel. In this wavelength band, the total intensity is almost an order of magnitude lower than that of the 2.49 μm band, and the range in intensity is not as great (see Figure 8a). The polarization angle in Figure 8b exhibits a continuous curve at the smaller scattering angles, unlike the data at 2.49 μm. This may be explained by the fact that the spectral sensitivity of the instrument is starting to fall off in the shorter wavelength region. Figure 8c shows that while the total intensity in this band is significantly lower than that in the 2.49 μm band, the percent polarization is substantially higher. The measured peak polarization of 30-60% in the 3.01 μm band seen in this figure confirms the earlier discussion that this band is highly absorptive and therefore the scattered signal has most likely undergone only a single scattering. This results in a more highly polarized signal.

5. POLARIZATION MODELING

As an initial attempt to explain the major features of the polarization data we tried several elementary models for atmospheric scattering by ice grains, e.g., that of a single reflection from a flat plates of ice (hereafter "platelet"). The platelets are taken to have smooth parallel surfaces and to be much larger in diameter than the wavelength of the radiation being studied, so that diffraction effects can be ignored. We also consider front surface reflection from hexagonal crystals.

We then simulate, via Monte Carlo techniques, what intensity the aircraft polarimeter would detect in each of its four orientations, for each position of the aircraft in its approximately circular trajectory (Figure 6a). To do this we utilize a large number of approximately monochromatic wavepackets of well-defined polarization, where the polarization is chosen randomly for each wavepacket. These wavepackets are assumed to come from the direction of the Sun and strike a single ice platelet; a certain fraction of the radiation is then reflected in the direction of the aircraft. We then know from this geometry exactly in which direction the normal vector to the ice platelet must be pointing. From Fresnel's equations we compute the reflected components of the E field, both parallel and perpendicular to the plane of incidence. Reflection from the
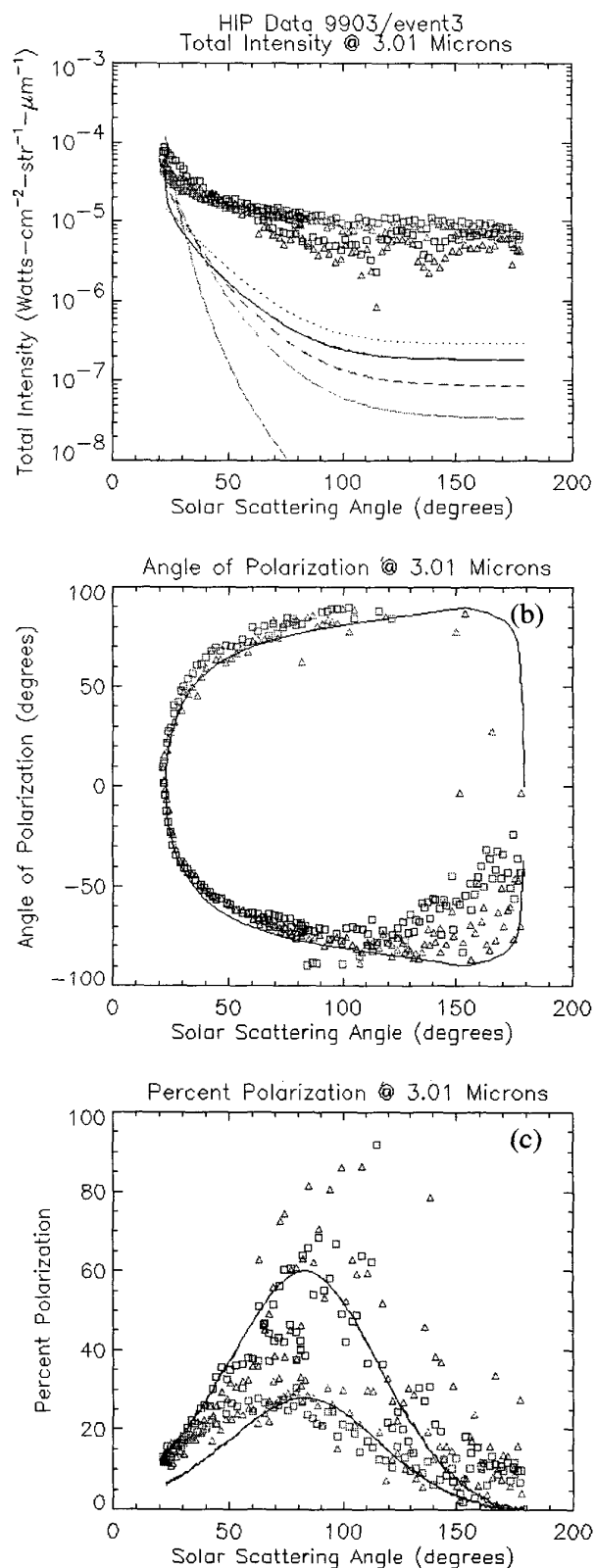

Figure 8. HIP Data for 3.01 μm: a) Total Intensity, b) Angle of Polarization, c) Percent Polarization

380

front and back surfaces, interference effects, and absorption within the platelet are taken into account. Tabulated values of the imaginary part of the index of refraction, interpolated to the desired wavelength, are used to determine the absorption

The components of both the parallel and perpendicular components of the E field are then projected onto the transmission axis of the polarizer; this is done for each of the four angles used to sample the incident flux. The resultant E field transmitted through the polarizer at each setting and the corresponding intensities are recorded.

This procedure is repeated for each of 10^4-10^5 simulated wavepackets, and the total intensity at each of the four polarizer orientations is summed. Then, according to equations (1), (2), and (3), we compute the percent linear polarization (P), the angle of polarization (A), and the total intensity (I). A polarization angle of zero corresponds to an alignment with the long axis of the aircraft. We repeat this evaluation of A, P, and I, for each of 360 evenly spaced positions of the aircraft in its orbit about the cloud field under study.

Single Scattering from Platelets

In these calculations, we take the normal vector to the platelets to be defined by the vectors from the Sun to the platelet and from the platelet to the aircraft as shown in Figure 6a. The normal vectors are invariably tilted at some angle, θ, with respect to the vertical - the nominal free-fall equilibrium position of the platelets. In order to compute an absolute value for the total intensity, I, we must know the probability of finding platelets tilted at various angles, θ. Somewhat arbitrarily we take this probability to be:

$$\frac{dP}{d\Omega} \approx \frac{e^{-\theta^2/2\sigma^2}}{2\pi\sigma^2} \qquad (4)$$

where σ is the rms tilt angle; the normalization holds only if $\sigma \ll 1$ radian. We have found that in order for our model calculations to approximately match the HIP data a value for σ of >30 degrees is required (see discussion below). This results from the fact that for most portions of the aircraft orbit, the scattered light from a single platelet would require large tilt angles (e.g., > 50 degrees). We therefore also consider a random distribution for the normal vectors to the platelets, i.e.,

$$\frac{dP}{d\Omega} \approx \frac{1}{2\pi}. \qquad (5)$$

As a final note about the grain properties, we take each wavepacket to encounter a grain whose thickness is chosen from a uniform distribution between values of 10 and 40μm.

Some portion of the calculations described above which were designed to simulate the polarization parameters vs solar scattering angle could have been carried out analytically, as opposed to utilizing Monte Carlo techniques. However, we were aiming to develop more general methods to be able to deal with the more realistic case of multiple scattering (see below).

Of the three quantities that we calculate from this simple model, A, P and I_{tot}, we utilize only two adjustable parameters. The polarization angle requires no adjustable parameters. The total intensity is found from the solar radiance and the assumption that there is a sufficiently high density of platelets so that every photon encounters at least one of them before passing through the cloud; however, the rms tilt angle used to determine the probability of finding a platelet with a given tilt is essentially a free parameter which we adjust to best match the data. In computing the percent polarization to compare with the observations we allow for an additional unpolarized component (unaccounted for in our simple model) which is also an essentially free parameter, but one that is held constant for all solar scattering angles.
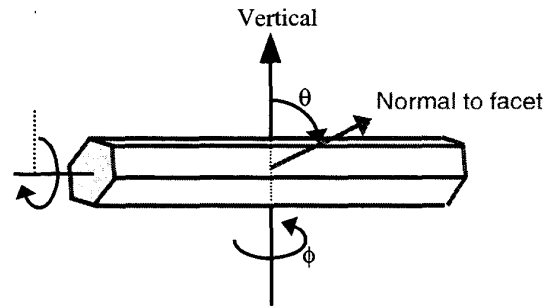

Figure 10. Definition of axes for hexagonal rod.

Single Scattering from Hexagonal Rods

Because of the rather large values required for the rms tilt angle in the platelet model, we also considered a model for the ice grains which involves long hexagonal rods. These have the advantage of having six surfaces to reflect light, and hence a greater probability for the light to encounter a surface with the required large tilt angles. Here we assumed that the rods float with their long axes essentially horizontal in the atmosphere (the orientation with maximal hydrodynamic stability). We take this axis to be randomly oriented in the horizontal plane (call the orientation in this direction ϕ; see Figure 10). If an orthogonal axis is chosen to be the normal to any one of the six surfaces, the angle between this axis and the vertical is defined to be θ. For θ and ϕ, each taken to be randomly distributed, we can compute analytically the probability of finding the normal to one of its surfaces with a tilt angle θ (with respect to the vertical). The probability is given by

$$\frac{dP}{d\Omega} = \frac{1}{\pi^2 \sin\theta} \qquad (6)$$

We have used this expression, in addition to the physics and geometry discussed above for simple platelets, to compute the expected polarization parameters for radiation undergoing single reflections from the surfaces of hexagonal ice crystals. No account is taken for transmission through, or internal reflections from, these crystals. This is beyond the scope of the present work and will be considered in future studies.

In this simple, front-surface, single scattering model neither the polarization angle nor the percent polarization depends on the grain orientation probabilities $(dP/d\Omega)$ or on the solar flux, $F_s(\lambda)$. However, in computing the overall scattered intensity as a function of SCA we utilize both of these in the following expression:

$$I(\lambda) = \frac{\xi\, F_s(\lambda)\dfrac{dP}{d\Omega}\sin\theta_s}{4\sin\theta_a} \quad \text{Watts/(cm}^2\text{-sr-}\mu\text{m)} \qquad (7)$$

where $F_s(\lambda)$ is in units of Watts/(cm^2-μm), θ_s and θ_a are the solar elevation and aircraft roll angles, respectively, and $dP/d\Omega$ is evaluated for the tilt angle of a crystal facet normal which is determined by the position of the Sun and the aircraft viewing geometry at a particular time and SCA. The factor of 4 in the denominator takes into account the fact that a shift in angle by an amount $\Delta\theta$ in the crystal facet normal corresponds to the deflection of a reflected ray by $\Delta\theta' = 2\,\Delta\theta$. In two angular dimensions this translates to $\Delta\Omega' = 4\,\Delta\Omega$. The factor ξ is included to take into account the fact that we are considering only single scattering, while in reality a photon typically has more than one chance to successfully reflect from an ice grain surface, especially at wavelengths near 2.5 microns (see the following discussion on multiple scattering). In the simulations described in Section 6 we take $\xi = 4$ for the 2.49 μm case, and $\xi = 1$ for 3.01 micron radiation.

Multiple Scattering from Platelets

Finally, we have carried out some preliminary investigations of multiple scattering, utilizing the simple platelet model. Figure 11 shows some of the possible interaction processes. A photon can be reflected from the front surface of a platelet, pass entirely through it, be internally reflected, or absorbed. A photon can do all of these repeatedly, except for absorption. We devised a simple Monte Carlo scattering code to follow a large number of photons which impinge on the scattering cloud. Each photon is followed until it (a) emerges back out of the cloud, or (b) is absorbed. At each surface that a photon encounters, a Monte Carlo "decision" is made as to whether that photon is transmitted or reflected. If transmitted into a grain, another decision is made as to

whether the photon is absorbed or not in transiting the grain. No attenuation of the radiation is considered outside of the platelets, e.g., due to the atmosphere or water vapor. The polarization is followed at all steps.
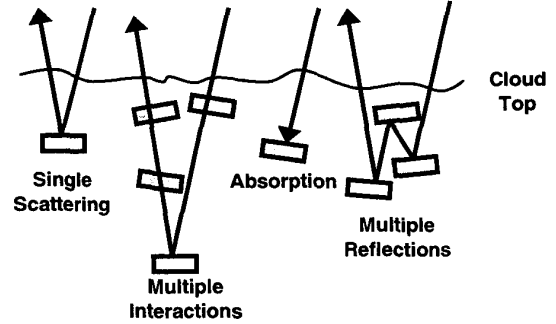

Figure 11. Multiple Platelet Scattering in 3-D

Our main purpose in carrying out such a multiple scattering calculation is to try to understand the degree of polarization as a function of wavelength that is observed in the HIP data. We find from the observations that the maximum percentage polarization at 3.01 μm is about 30 - 60%, whereas at 2.49 μm it is limited to about 10% (see Figures 7c and 8c). The qualitative explanation for this effect is that radiation near 3 μm is heavily absorbed in ice; therefore, only reflections from a single surface are likely to lead to the photon's escape from the cloud, as opposed to a route via multiple interactions. Therefore, this mostly singly reflected radiation is likely to retain a larger fraction of the polarization induced by reflection.

To help quantify the number of scatterings and interactions we simulate 10^5 photons impinging at a fixed incidence angle on the cloud, and follow them until they either emerge from the cloud or are absorbed. We compute the number of photons that emerge from the cloud according to the number of reflections a photon makes and the number of interactions it has. The distinction here is that "interactions" refers to the number of platelets that a photon interacts with, even if such an interaction consists of nothing more than passing completely through it. In the simple platelet model, passage through the grain does not change the direction of the radiation or its direction of polarization. Thus, such a simple interaction would neither enhance nor decrease the degree of polarization. Nonetheless, for more realistic crystal shapes, passage into or through the crystal would almost certainly change the direction of propagation and the direction of polarization. Therefore, we regard these initial exploratory calculations as simply providing some insight into what would happen with more complex shaped crystals.

Some sample results of this study are shown in Figures 12 and 13. In Figure 12 we show the number of photons reflected back out of the cloud as a function of photon wavelength. The various curves show the percentage of photons emerging from the cloud (I_{tot}), the percentage that

have "interacted" with only a single platelet (I_{sing}), the percentage that have interacted with more than one platelet (I_{mult}), and the ratio I_{sing}/I_{mult}. One sees that for wavelengths above 2.75 μm, almost all the photons escaping the cloud have interacted with only one platelet. This is to be expected because of the high degree of absorption; hence any photon entering a platelet is very likely to be absorbed. For shorter wavelengths, just the opposite is true, and most of the photons interact with more than one platelet. This is a first step toward explaining the larger degree of polarization observed at the longer wavelengths.
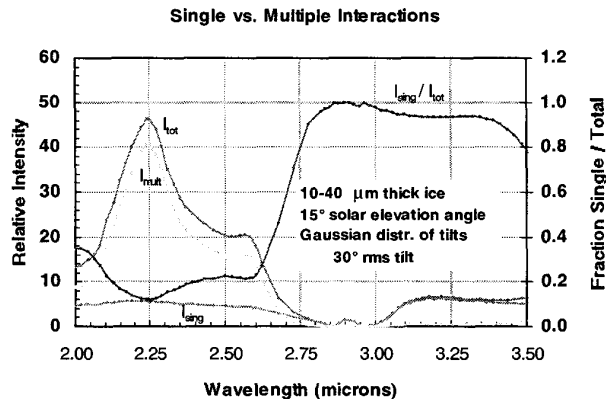
Single vs. Multiple Interactions

Figure 12. Single Vs. Multiple "Interactions" of photons in an ice field.
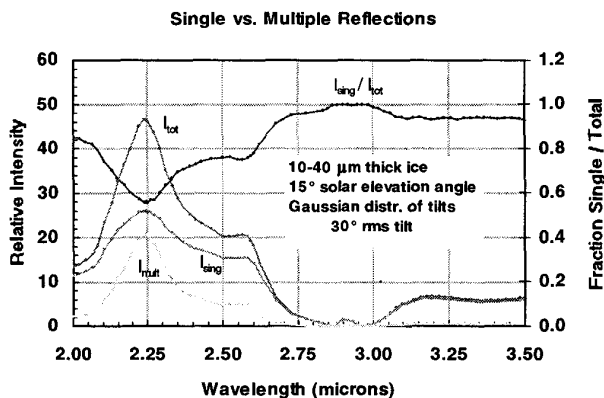
Single vs. Multiple Reflections

Figure 13. Single vs. Multiple Reflections of photons in an ice field.

To complete this simple picture, we show in Figure 13 the same type of plot as in Figure 12 except that here the actual numbers of *reflections*, as opposed to any interaction with a platelet, are considered. Note that when only reflections are considered, the contrast between the ratio of singly reflected to multiply reflected photons at longer wavelengths and that at shorter wavelengths is not nearly as great as was evident in Figure 12. As mentioned above, however, for more realistic crystal geometries, a simple passage through a crystal can substantially alter both the propagation and polarization directions. Thus, the actual fraction of photons whose polarization angle is *not* determined by the apparent

scattering angle (defined by the sun-cloud and cloud-detector vectors) probably lies between that implied by Figure 12 and that of Figure 13. Clearly, this type of calculation needs to be repeated for more realistic scatterers.

6. COMPARISON OF HIP DATA AND MODEL

A comparison of the single scattering model discussed in the previous section with the HIP data is displayed in Figures 7 and 8. The various curves superposed on the data are the results of the model calculations. The angle of polarization derived from the model, as discussed earlier, is a function of the geometry of the observation. The solid curves in Figures 7b and 8b show the model in comparison with the data. In the 3.01 μm case, the model appears to run nicely through the data; however, at 2.49 μm, it does not do as well. We believe this may be indicative of low signal to noise in the data. As mentioned earlier, the spectral response of the instrument goes through a transition in sensitivity at the shorter wavelengths. However, we plan to further investigate this discrepancy.

Turning our attention to the model-data comparison for percent polarization (Figures 7c and 8c), we note that the data in both bands exhibit maximum percent polarization at scattering angles different from what is predicted by the model. The model was simply normalized in amplitude to fit the data. If the data contained more than one peak (as in the 3.01 μm case), then two representative model curves are shown. The model clearly predicts a maximum percent polarization at approximately 77 degrees for 2.49 μm and 90 degrees for 3.01 μm. These predicted peaks correspond simply to angles of incidence equal to the Brewster angles (which depend on the index of refraction).

Finally, a comparison of the HIP data and several model predictions for total intensity is shown in Figures 7a and 8a. The long dashed curves (red, green and blue) in these figures correspond to the simple platelet model with rms tilt angles of 20°, 30°, and 40° respectively. The short dashed curve represents platelets with random orientations, while the solid curve corresponds to the model simulating contributions from hexagonal rods (both described in Section 6). For 2.49 μm, while the latter two models match the total intensity values fairly well at the minimum scattering angles, they are off by up to factors of approximately 3-5 at other SCA's. Given the simplicity of our model, even this level of agreement is encouraging.

Examination of the 3.01 μm model comparisons with the data, however, shows that they do not do nearly as well as in the 2.49 μm case. In the 3.01 μm case, the models do a much poorer job predicting the total intensity throughout most of the SCA range; the modeled intensity is more than one order of magnitude lower than the data. In view of the fact that reflection at normal incidence at 3.01 μm is only ~10^{-3}, and that for SCA's near 180° any front surface

reflections must be near normal incidence, it is difficult to understand the large intensities in the 3 μm band at the large SCA's. Furthermore, due to the large absorption cross section in ice at these wavelengths, internal reflections from ice crystals should be minimal.

7. CONCLUSIONS

The HIP instrument has been described in some detail here. Both the instrument and the processing techniques used on the data have been discussed. Spectral measurements (at 0.03 μm resolution) in the 2.5 – 3.5 μm range of the total cloud intensity, the percent polarization, and polarization angle were collected. The polarization properties show significant wavelength variation, so these spectral measurements are valuable in understanding and modeling the processes taking place during scattering.

The HIP sensor as flown on FISTA98 does not have sufficient sensitivity to make polarization measurements of the clouds using single pixels from individual frames. Averaging of pixels in the temporal and spatial domains proved to be an effective way of averaging out some of the sensor noise and thereby greatly improve the quality of the polarization measurements.

However, we surmise that the coadding process has not sufficiently suppressed the statistical and systematic effects in the data at all SCA's. This supposition is based on the behavior of both the angle of polarization and percent polarization results. Specifically, we note the ragged appearance of the angle of polarization plots exhibited by the mixture of color in the plots (from different sides of the orbit). The somewhat random switching of angle from positive to negative values in successive data points is not physically meaningful. In addition, the distribution of data points in the plots of percent polarization as a function of SCA shows a significant amount of spread which may be indicative of residual system noise. SDL is currently building an improved sensor to be used in future HIP flights, which will provide data at substantially higher spatial and time resolution.

We have found that the angle of polarization results could be readily interpreted by our simple single scattering model. As stated earlier, the polarization angle is largely dependent on the viewing geometry. The modeled total intensity (while not specifically a property of polarization) was found to match reasonably well to the 2.49 μm data, but failed to explain the substantial 3.01 μm intensity at large SCA's. Finally, at both wavelengths studied, the percent polarization as a function of SCA generated by the model qualitatively matches that of the data. However, the model does not predict the magnitude of the peak polarization, and it predicts the peak to occur at solar scattering angles significantly different from what is seen in the data.

These results indicate that our simplified polarization model will have to be upgraded to include more complex ice grains and scattering processes in order to more accurately model the effects of polarization induced through scattering from clouds. In addition, we look forward to comparing results of this model to data to be obtained using the new HIP sensor.

8. REFERENCES

[1] George W. Kattawar and Gilbert N. Plass, "Degree and Direction of Polarization of Multiple Scattered Light. 1: Homogeneous Cloud Layers", Applied Optics 11, 2851-2865, December 1972.

[2] R.A.R. Tricker, Introduction to Meteorological Optics, New York: Elsevier, 1970.

[3] Robert Greenler, Rainbows, Halos, and Glories, Cambridge, England: Cambridge University Press, 1980.

[4] Yoshihide Takano and Kuo-Nan Liou, "Solar Radiative Transfer in Cirrus Clouds. I - Single-Scattering and Optical Properties of Hexagonal Ice Crystals", Journal of Atmospheric Sciences 46, 3-19, January 1, 1989.

[5] Yoshihide Takano and Kuo-Nan Liou, "Solar Radiative Transfer in Cirrus Clouds II - Theory and Computations of Multiple Scattering in an Anisotropic Medium", Journal of Atmospheric Sciences 46, 20-36, January 1, 1989.

[6] James E. Hansen, "Multiple Scattering of Polarized Light in Planetary Atmospheres. Part 2: Sunlight Reflected by terrestrial Water Clouds", Journal of Atmospheric Science 28, 1400-1426 , November 1971

[7] George M. Hale and Marvin R. Querry, "Optical Constants of Water in the 200-nm to 200-μm Wavelength Range", Applied Optics 12, 555-563, March 1973.

[8] Joel W. Schaaf and Dudley Williams, "Optical Constants of Ice in the Infrared", Journal of the Optical Society of America 63, 726-732, June 1973.

[9] Gary L. Jensen and James Q. Peterson; "Hyperspectral imaging polarimeter in the infrared," Proceedings of the SPIE Conference on Infrared Spaceborne Remote Sensing VI, 3437, 42-47, July 1998.

[10] W.S. Bickel and W. M. Bailey, "Stokes vectors, Mueller matrices, and polarized scattered light," American Journal of Physics, 53 (5), May 1985, pp. 468-478.

[11] D.S. Kliger, J.W. Lewis, and C.E. Randall, Polarized Light in Optics and Spectroscopy, Academic Press, 1990.

[12] R.A. Chipman, "Polarimetry," in M. Bass (ed.), *Handbook of Optics*, 2d ed., McGraw Hill/OSA, 1994, Vol II, Chap. 22.

[13] L.J. November and L.M. Wilkins, "Liquid crystal polarimeter: a solid state imager for solar vector magnetic fields," *Optical Engineering*, Vol. 34, No. 6, 1995, pp. 1659-1668.

[14] James Q. Peterson, Gary Jensen, Joe Kristl, and Mark Greenman, "Calibration of the Hyperspectral Imaging Polarimeter", submitted to the SPIE Conference on Polarization: Measurement, Analysis, and Remote Sensing II, July 1999.

9. BIOGRAPHY

Cynthia J. Beeler is a Senior Scientist at Visidyne, Inc. and specializes in the analysis of remote sensing data for the application to multi-spectral phenomenology. She is accomplished in signal analysis and image processing with a particular focus in characterizing background spatial structure. Most recently her work has involved geographical registration of satellite imagery, 3D scene construction of stereo satellite images, and stereo tracking algorithms. Ms. Beeler was the project leader for the development and application of the high-throughput MSTI-3 data image processing and analysis software (ASAP), and was a co-investigator for other Earth Backgrounds Experiments on the MSTI program.